An Experimental Investigation of Capillary Driven Flow in Open Rectangular Channels:

A Method to Create PDMS Microfilaments for pN Scale Force Measurements

by

Timothy Wayne Sowers

A Thesis Presented in Partial Fulfillment
Of the Requirements for the Degree
Master of Science

Approved May 2014 by the
Graduate Supervisory Committee:

Jagannathan Rajagopalan, Chair
Marcus Herrmann
Huei-Ping Huang

ARIZONA STATE UNIVERSITY

August 2014

ABSTRACT

The flow of liquid PDMS (10:1 v/v base to cross-linker ratio) in open, rectangular silicon micro channels, with and without a hexa-methyl-di-silazane (HMDS) or poly-tetra-fluoro-ethylene (PTFE) (120 nm) coat, was studied. Photolithographic patterning and etching of silicon wafers was used to create micro channels with a range of widths (5-50 μm) and depths (5-20 μm). The experimental PDMS flow rates were compared to an analytical model based on the work of Lucas and Washburn. The experimental flow rates closely matched the predicted flow rates for channels with an aspect ratio (width to depth), p, between one and two. Flow rates in channels with p less than one were higher than predicted whereas the opposite was true for channels with p greater than two. The divergence between the experimental and predicted flow rates steadily increased with increasing p. These findings are rationalized in terms of the effect of channel dimensions on the front and top meniscus morphology and the possible deviation from the no-slip condition at the channel walls at high shear rates.

In addition, a preliminary experimental setup for calibration tests on ultrasensitive PDMS cantilever beams is reported. One loading and unloading cycle is completed on a microcantilever PDMS beam (theoretical stiffness 0.5 pN/ μm). Beam deflections are actuated by adjusting the buoyancy force on the beam, which is submerged in water, by the addition of heat. The expected loading and unloading curve is produced, albeit with significant noise. The experimental results indicate that the beam stiffness is a factor of six larger than predicted theoretically. One probable explanation is that the beam geometry may change when it is removed from the channel after curing, making

assumptions about the beam geometry used in the theoretical analysis inaccurate. This theory is bolstered by experimental data discussed in the report. Other sources of error which could partially contribute to the divergent results are discussed. Improvements to the experimental setup for future work are suggested.

DEDICATION

I would like to dedicate this thesis to my family. Without their love and support, this thesis would have never come into being. Thanks Mom and Dad for everything you've done for me.

ACKNOWLEDGEMENTS

TABLE OF CONTENTS

LIST OF FIGURES

NOMENCLATURE

a   flow speed constant, $a = \sqrt{k}$

A   Cross sectional area of beam

A_D area of beam acted on by vertical natural convection currents

b   width of beam

C_D drag coefficient

d   channel depth

E   Young's Modulus

F_B net buoyancy force on beam

F_D drag force on beam due to natural convection currents

g   gravitational constant

g(t)   geometric parameter for analytical flow model

h   height of beam

I   Moment of Inertia of beam

k   "mobility parameter"

L   length of beam

p aspect ratio, channel width/depth

$\Delta P/x$ pressure gradient due to capillary force

q   distributed load on beam due to buoyancy force

t   time, sec

$\vec{u}$ fluid flow velocity vector

v flow velocity in x-direction

v	velocity of water due to natural convection
V	Volume of beam
w	channel width
x	distance traveled by fluid
y	vertical position from bottom of channel
z	horizontal distance from middle of channel
δ	deflection of free end of beam
γ	surface tension, mN/m
μ	dynamic viscosity, Pa s
ρ	density
θ	equilibrium contact angle

INTRODUCTION

Soft materials such as polydimethylsiloxane (PDMS) have proven useful for researchers [1] developing microfluidics devices. The unique physical properties of PDMS have made it a material of choice for many researchers. It has a low Youngs modulus (~1 MPa) [2], is optically transparent at visual wavelengths, and is relatively cheap. It can also be used at wide temperature ranges [3] and is biocompatible [4].

A variety of PDMS based devices and sensors have been developed. Arrays of PDMS microstructures have been used to measure forces at the cellular level [5,6] after it was shown that mechanical forces between cells directly affect their growth and migration [7]. This is only one example of the increased use [8,9] of PDMS based devices in the area of mechanobiology, which studies the effect of the mechanical microenvironment on cell and tissue behavior. PDMS microstructures have been designed to measure flow rates in microfluidics systems [10], and to create micro valves and pumps [11]. PDMS based micro devices have been used extensively to study biological systems [12,13]. Due to its unique advantages, novel applications for PDMS devices, such as self-propelled biohybrid swimmers [14], continue to be developed.

The process of capillary micromolding can be used to form micrometer-length scale polymeric structures in a way that is easily repeatable and produces reliably shaped devices [15,16]. The polymeric, mask like structures were first formed [15,16] by placing an elastomeric stamp in contact with a substrate, which formed a network of channels. A liquid is then placed by the channel entrance, where it is pulled into the channel by capillary action and solidifies into the desired pattern. A complimentary

fabrication method for PDMS devices with very large length to width/depth ratios (~500:1) has been recently reported [4]. In this process micro channels are etched into a silicon substrate using lithography. Liquid PDMS is injected into a reservoir, and pulled by capillary force into micro channels which have been etched into the shape of the desired device. The PDMS device is removed from the channels after curing. Using this method, extremely sensitive cantilevers with stiffnesses less than 0.1 pN/μm and micro platforms for cell biology can be created [4]. In addition, more complex devices could be developed. The potential designs for such devices are theoretically infinite, although two such examples can be found in the literature [17,18]. In one such example [17], the force sensor consists of a set of linear beams connected in series. The advantage of these devices would be a linear stress-strain profile at larger strains, since each individual beam would have a smaller displacement than the device as a whole.

As a device becomes longer and more complex, it becomes necessary to deposit a non-adhesive layer (e.g. Teflon, HMDS) on the silicon wafer so the device is not damaged upon removal. However, the non-adhesive layer significantly slows the capillary flow of the liquid PMDS, which ultimately constrains the possible device geometries. Generally, the flow behavior of PDMS in these open rectangular micro channels follows the Lucas-Washburn [19,20] equation, in which the square of the distance traveled is proportional to time, $x^2 \sim t$. For a given surface layer, the width, depth, and width/depth ratio of the channel will affect the capillary flow rate. Researchers have reported varying impacts on flow behavior as a result of some of these parameters. For example, one researcher reported that the channel filling time is sensitive to channel depth only up to a certain threshold for a given width [21]. Another

researcher has theorized the effect of forward meniscus morphologies on flow rate [22] in vertical micro channels, but a full investigation was outside the scope of his work. An additional researcher measured the effect of forward meniscus morphologies in rough versus smooth micro channels [22] at very short time scales. A complete understanding of the conditions under which these parameters will impact capillary flow rate is currently lacking.

In the first part of this work, a more comprehensive set of tests is designed to determine the parameters affecting the flow rate of PDMS in micro channels. The tests were completed in open rectangular micro channels with depths of 5-20 μm and widths of 5-50 μm. The flow rate is compared to a simplified flow model [24] based on the Lucas-Washburn equation [19,20]. It should be noted that a similar derivation for the flow rate in a vertical open rectangular micro channel has also been reported by Ouali et al.[22]. Analytical and numerical solutions for capillary driven steady evaporating flow in open, rectangular micro channels have also been found [25]. Generally, the model predicts the experimental results quite accurately for channels with p between one and two. However, experiments show that the flow rate diverges from the model predicted values based on the distinct forward meniscus morphology, which is dependent on equilibrium contact angle and the width/depth ratio [26] of the channel, at large with to depth ratios. This effect becomes greater as p increases. In addition, it is argued that a curved top meniscus slows the flow at small channel depths when p is greater than one. This effect arises because a concave down meniscus will reduce the cross sectional area in which PDMS will flow, thus increasing viscous forces arising from the liquid surface interactions at the

wall. Finally, in low aspect ratio channels with high shear rates, faster flow rates may be caused by partial slip at the walls.

In the second part of this work, a preliminary experimental setup for calibration tests on the types of beams described in [4] is reported. One loading and unloading cycle is completed on a microcantilever PDMS beam with a length of about 2.8 mm, a depth of 10 μm, and a width of 20 μm. The beam does not have sufficient strength to support its own weight in air, so it is suspended in water which has a similar density to cured PDMS. Beam deflections are actuated by adjusting the buoyancy force on the beam. The buoyancy force is adjusted by increasing the temperature of the water, which decreases the water density. Preliminary results show the general trend expected for a loading and unloading cycle, albeit with significant experimental error. The error is a result of the extreme sensitivity of the beam, which based on its design should have a stiffness of about 0.5 pN/μm according to Euler beam theory. The experimental results indicate that the beam stiffness is a factor of six larger than predicted theoretically. One probable explanation discussed is that the beam geometry may change when it is removed from the channel after curing, making assumptions about the beam geometry used in the theoretical analysis inaccurate. This theory is partially bolstered by images taken of beams that have been removed from the channel in which they were cured using an electron microscope on campus. A second probable explanation is that errors in estimating the beam length are causing artificially small theoretical beam deflections. Several sources of error which could also partially contribute to the divergent results are described. Improvements to the experimental setup that could mitigate the effect of these sources of error in future experiments are suggested.

EXPERIMENTAL METHODS

A. Flow Experiments

A.1 Micro Channel Fabrication

Silicon wafers were prepared using standard lithography techniques. Photoresist was spin coated on the silicon wafer. The photoresist (3 microns) was applied using a photoresist spinner in a class-100 clean room. The wafer was then aligned with a chrome mask (minimum feature size 2-2.9 micron, critical dimension tolerance +/- 0.3 microns) and exposed to UV light to transfer the pattern onto the photoresist. Anisotropic Reactive Ion Etching (SF_6) was used (Oxford Instruments Plasmalab 80+ RIE (F)) to create rectangular channels in the silicon wafer.

Experiments were conducted on wafers with a polytetrafluoroethylene (PTFE) coating or uncoated Silicon. Polytetrafluoroethylene was deposited (STS ICP Advanced Silicon Etcher) over two minutes to achieve a 120 nm coating. Experiments were also conducted on HMDS coated wafers. The HMDS coat was applied with same spinner that was used to apply the photoresist.

A.2 Experimental Setup

Liquid PDMS was injected into a large reservoir within 10 minutes of mixing. In Figure 1a, the reservoir is shown on the left and the dark advancing contact line of PDMS is just visible. Horizontal micro channels with widths of 10, 20, 30, 40 and 50 μm were

connected to the reservoir. Liquid PDMS is visible in the reservoir of the left. Rectangular notches in between channels are used as 1 mm distance markers. After injection, the PDMS contact line will expand until it reaches the front edge of the capillaries.

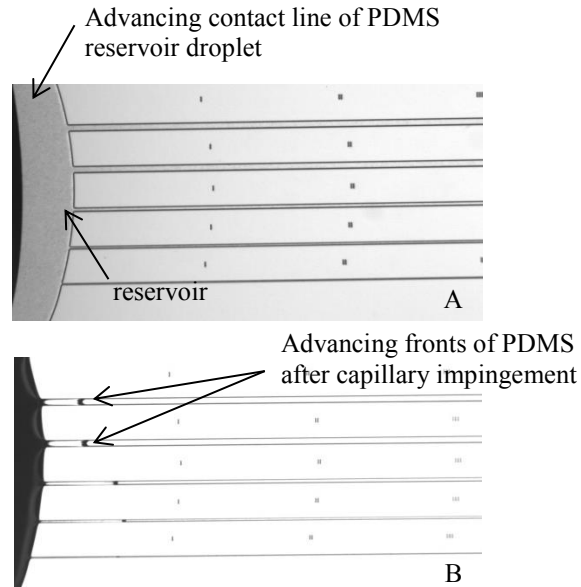Figure 1. Two Frames of Video Taken during Flow Experiments.

In Figure 1b, five channels are shown after PDMS impingement on PTFE. The experiments were video recorded (ThorLabs digital CMOS camera) until the fluid travels about 3 mm in each channel. If the flow rate was slow, the video was stopped after 30-40 minutes. A minimum resolution of 1.06 μm/pixel was required to track the capillary flow in the narrowest channels.

A.3 Data Analysis

Video was recorded at a rate of 1 frame per second, and then converted to a sequence of images. The forward meniscus was tracked using the cpcorr function found in the image processing toolbox in MATLAB. The code used is included in Apprendix A. For some experiments, long fingers of PDMS extended into the channel. Since the manufacture of PDMS devices requires complete filling of the channel before curing, the bottom of the meniscus was tracked. In micro channels with large widths and small depths, long forward menisci were present. The calculated flow rates could be artificially low in these flow regimes as a result. The data was then fitted to the general equation

$$x = a\sqrt{t} \tag{1}$$

for capillary flow [19,20], with an offset for the initial time and initial meniscus location. The average value of the flow rate constant, a, was calculated from an average of three experiments. Error bands were defined as the maximum and minimum value for a given experimental condition. These values were compared to a simplified analytical model [24] for capillary flow, based on the work of Lucas and Washburn[19,20].

A.4 Liquid Properties

The viscosity of Dow Corning Sylgard 184 has been reported to increase from 4.050 Pa s at a shear rate of 2 s^{-1} and 4.150 Pa s at a shear rate of 30 s^{-1} [27]. A constant value of 4.050 Pa s [27] for PDMS at shear rates smaller than 5 s^{-1} was used. Shear rates

for PDMS were well below this limit for all but a few experiments near the channel wall. It should be noted that the viscosity of Sylgard 184 at room temperature will increase by about 8% over a 15 minute interval [27] shortly after mixing, so capillary flow experiments were always initiated within 10 minutes of mixing. The surface tension used for PDMS was 19.8 mN/m at 20 degrees Celsius [28].

A goniometer (rame-hart instrument co.) was used to measure the equilibrium contact angle of PDMS on silicon, PTFE, and HMDS. The equilibrium contact angle on PTFE was 30.4°. The equilibrium contact angle on silicon and HMDS was so small (<5°) it could not be reliably calculated by the goniometer. Thus, a contact angle of 0° was used in the model. The equilibrium contact angle appears in the model as the argument in a cosine term, so this caused negligible error. To check this assumption, model values were recalculated at 6° and it was found that the resultant error for each value was at most a few tenths of a percent.

A.5 Analytical Model

The analytical model is identical to that used by Yang et al. [24] for capillary flow in open rectangular micro channels. The following is a summary of the theoretical assumptions made in the derivation of this model. It is assumed that the flow rate follows the linear relation developed by Lucas [17] and Washburn [20]:

$$x^2 \approx k\,t \tag{2}$$

where x is the distance traveled by the flow, t is time, and k is a "mobility parameter" which depends on the channel geometry (width, depth, and shape), liquid surface tension and liquid viscosity. As the PDMS travels along the capillary, the surface free energy is decreased. The driving force of the flow is thus the negative rate of change in surface free energy versus the distance traveled by the flow. Drag force is caused by viscous friction within the capillary. Additional viscous drag at the channel entrance and forward meniscus are neglected in this model.

The reservoir droplet has a diameter of 2-3 mm, giving it a large radius of curvature. As such, the Laplace pressure in the droplet is small so the assumption of flow driven by capillary force only is an accurate approximation. The model also assumes the channel is completely filled with a flat liquid profile at the top surface of the channel. The forward (in the direction of the advancing flow) meniscus is also assumed to be flat. Thus, the velocity profile is taken to be dependent on the y and z direction only for a given pressure gradient. Finally, the model assumes that the contact angle is constant, and can be approximated as the equilibrium contact angle.

Due to the small length scales and flow velocity, Stokes equation can be used to approximate the flow

$$\nabla^2 v = -\frac{\Delta P}{\mu\, x} \qquad\qquad \nabla \vec{u} = 0 \qquad\qquad\qquad (3)$$

where v is the flow velocity, μ is the dynamic viscosity, and the pressure gradient $\Delta P / x$ varies with the distance traveled by the flow. Solving these equations while assuming a

no slip boundary condition on the bottom and side walls and a free slip boundary condition [27] on the top surface gives the mobility parameter

$$k = \frac{2\gamma D}{\mu} \frac{2\cos\theta - (1-\cos\theta)p}{p^2} g(p) \tag{4}$$

with

$$g(p) = \frac{128}{\pi^5} \sum_{n\geq 0, nodd} \frac{1}{n^5} \left[\frac{n\pi}{4} p - \tanh\left(\frac{n\pi}{4} p\right) \right] \tag{5}$$

where p is the channel width to depth ratio, θ is the equilibrium contact angle, and g(p) is a geometric parameter that is completely dependent on the channel cross section.

B. Deflection Experiments

B.1 Microchannel Fabrication

See "A.1 Microchannel Fabrication" Section

B.2 Experimental Setup

Molds for the PDMS beams were manufactured using photolithography on a silicon wafer. The etching process was identical to that used to manufacture the silicon wafers for the micro channel capillary experiments. To ensure that the beams were

removed from the wafer molding without being damaged, the wafers were coated with PTFE after the etching process was complete.

Removing the PDMS beams from the wafer without causing damage or inelastic deformation required great care. A section of the wafer with a device was cleaved from the larger wafer and submerged in isopropyl alcohol (IPA). Due to its relatively large dimensions, the reservoir could be immediately separated from the wafer surface using tweezers without risk of damage. However, the small depth and width of the beams (tens of microns) make them much more fragile, so the wafer section was left to soak in the IPA for about an hour which reduced adhesion. The beams were then slowly lifted from the wafer by raising the reservoir upwards (Fig. 2), with the whole device still being submerged in IPA. In Figure 2, the IPA that would normally be present in the pitri dish to encourage separation was not added so that the PDMS devices would be clearly visible in this image. Three beams run between each pair of rectangular reservoirs. Some of these beams are just barely visible. PDMS begins to deform inelastically at a strain of about 0.5 [27], so the PDMS removal was undertaken slowly to keep strains on the PDMS at a minimum. The entire process of removing the PDMS device from the wafer took about 2-3 minutes when done correctly.
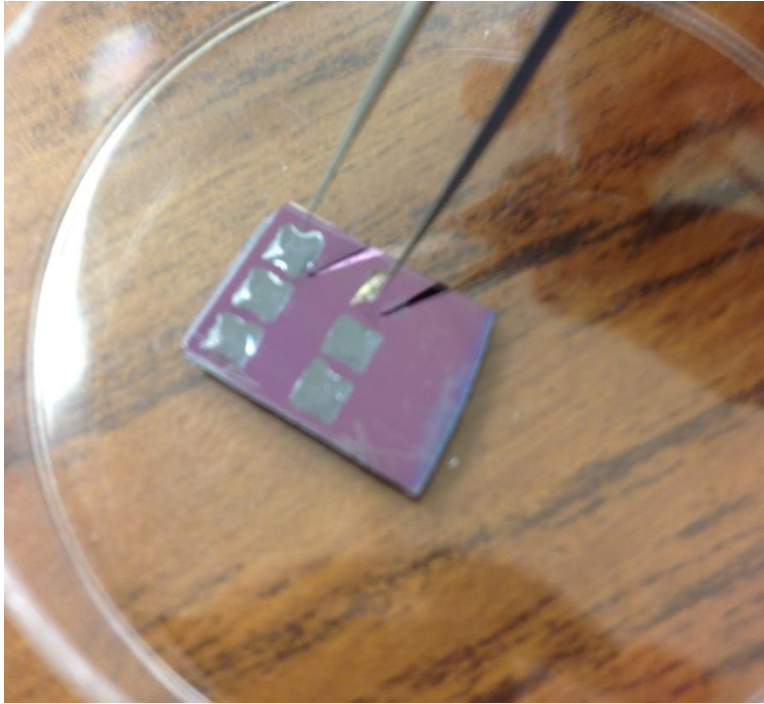
Figure 2. Beam Being Lifted off a PTFE Coated Wafer.

Once the device was completely removed from the wafer, it was transferred to a second, flat wafer section that was also submerged in the IPA. This section was then quickly lifted out of the IPA, with the device still on the top surface. On each of the devices, three individual beams are located between the two reservoirs. This was incorporated into the design so that if any beams were damaged while removing the device from the wafer, at least one beam would be intact for the experiment. To prevent entanglement during the deflection experiment, all but one PDMS beam is removed from the device once the device is removed from the wafer.

Figure 3. Test Substrate for the PDMS Beams.

Next, the device was moved to the test substrate (Fig. 3). The test substrate consisted of two flat platforms at different heights. Th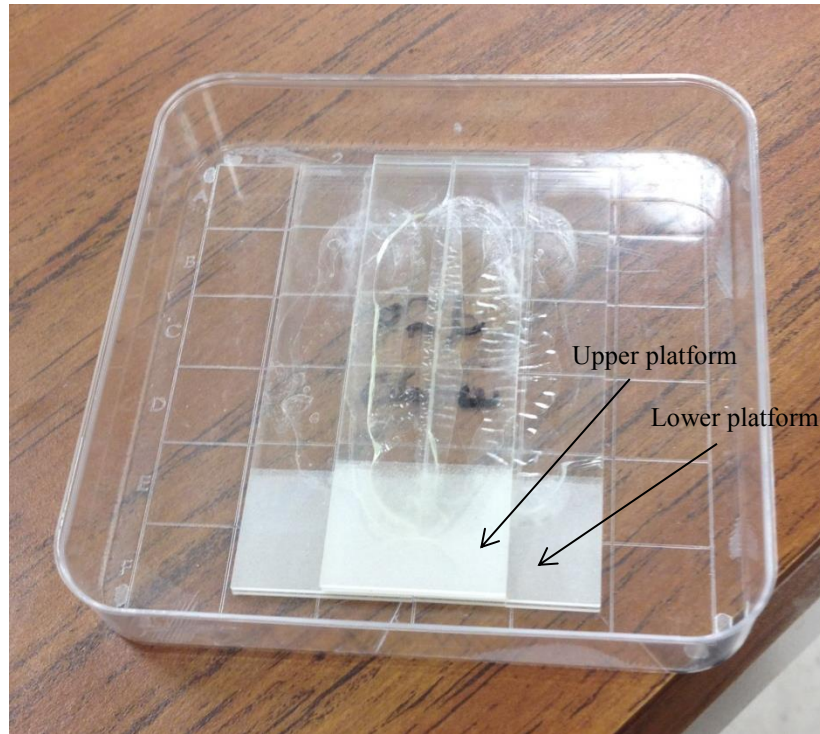e platforms were created using super glue to join several microscope glass slides. The first platform was formed using four slides. Two slides were placed with their long edges touching, and one slide was placed on top of each of them. The second platform consisted of two stacked slides, and was glued on top of the first platform. Once the platforms were glued together, the entire piece was super glued to the bottom of a plastic, square pitri dish. A square pitri dish was used so that the beam, once submerged in water, could be viewed from the side using a microscope without the curvature of the pitri dish distorting the image.

The device was then moved to the correct the substrate. The section with the pitri dish was placed adjacent to the device test location. Several drops of IPA were placed

onto the device to reduce adhesion between the device and wafer section as needed. Two tweezers were used simultaneously to grab the device, with each tweezer being used to grab one reservoir. The device was then pulled onto the platform test location. One reservoir is placed onto the second, uppermost platform such that the reservoir is at the edge with the beam hanging down toward the lower platform. The second reservoir is placed on the lower platform. It is located sufficiently close to the upper platform that the beam is not taut. The IPA is allowed to dry so that the reservoirs become stuck to the glass slide surfaces. The substrate is then moved to the microscope setup (Fig. 4).
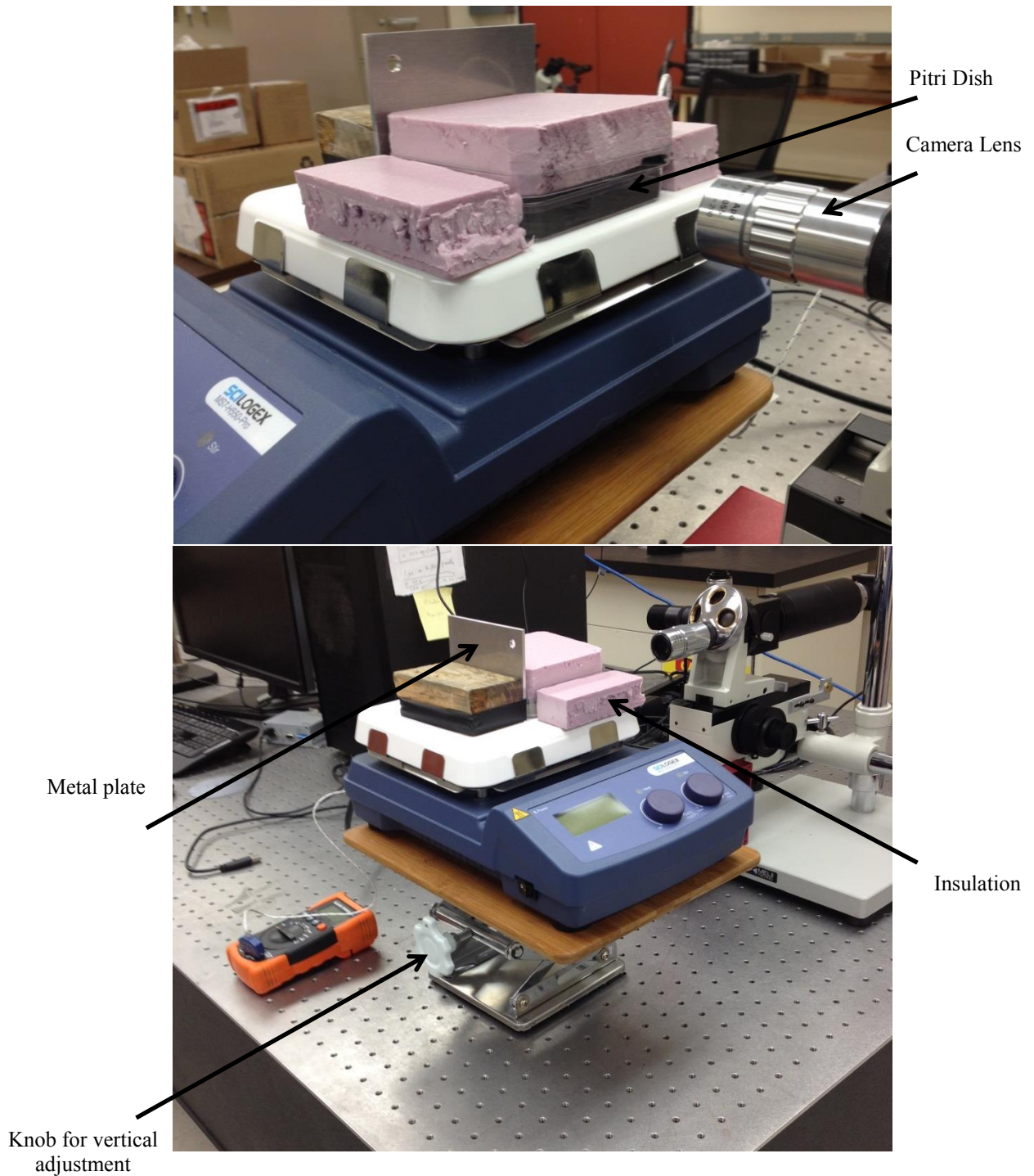
Figure 4. Microscope Setup used for Microcantilever Experiments.

Afterwards, distilled water is added to the pitri dish so that the beam is completely submerged. The lens is moved so that the PDMS beam is in focus. Due to the high

sensitivity of the PDMS beam, small disturbance in the water can cause large movements of the PDMS beam. These movements occasionally cause the beam to become damaged, so the water is allowed to settle for about 15 minutes. Afterwards, a razor is used to cut the beam near the reservoir located on the lower platform. Since the cured PDMS has a density near that of water at room temperature (1030 kg/m^3 [3] versus 1000 kg/m^3, respectively) the beam then slowly lifts so that it is approximately horizontal (Fig. 5).
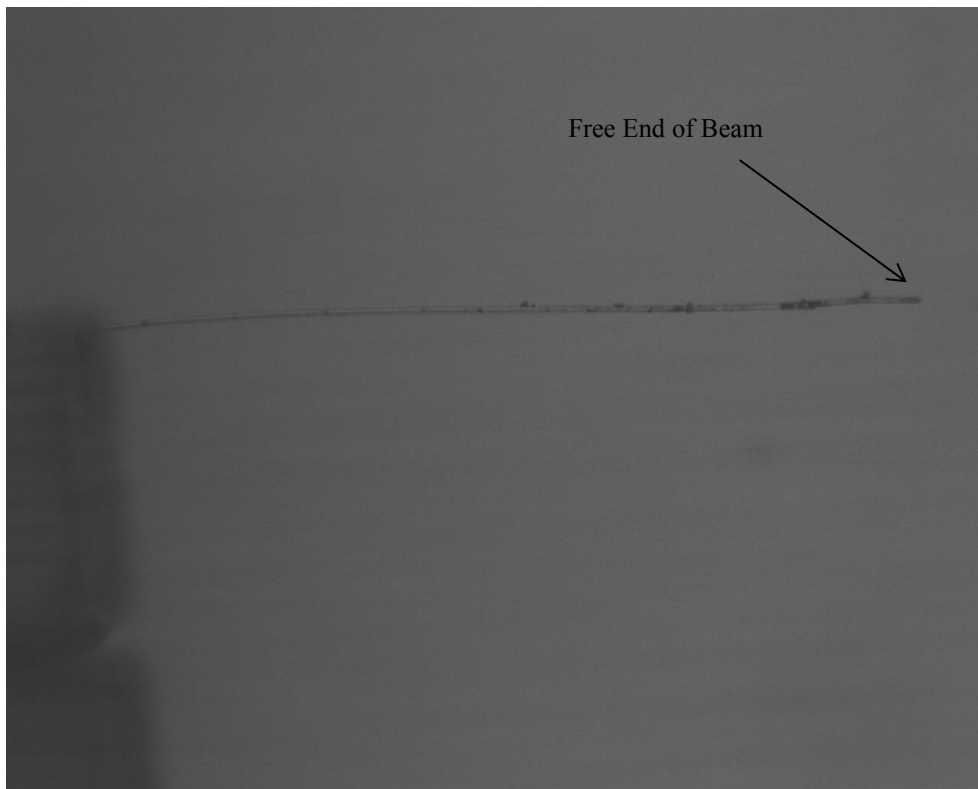

Figure 5. Image of a PDMS Beam Shortly after being Severed.

The microscope setup is shown in Figure 4. A video recording device (ThorLabs, resolution 2.649 µm/pixel) is used to capture the change in height of the free end of the PDMS beam as the water density is changed by heating. The camera is oriented

horizontally, and takes images of the PDMS beam through one side of the plastic pitri dish. The pitri dish containing the substrate and PDMS device is located on top of a hot plate (SCILogex MS7-H550-Pro) which in turn is placed on top of the metallic stand shown. A metallic plate is used to reflect light back to the camera lens, and is held vertical by taping it to the wood block shown in the picture. Initial experiments indicated a large temperature differential between the water and the surface of the hot plate. Since the plastic pitri dish will deform near 100˚C, this placed a lower limit on the range of water densities that could be used for the experiment. To increase the temperature range, insulation (Owens Corning, Foamular) was added to the setup. One piece is located at each side. In addition, a second piece is inserted into the top piece of the pitri dish, which functions as both a heat insulator and reduces evaporation. A thermocouple is also incorporated into the top piece to measure the temperature of the water. The thermocouple is placed so that its height in the water is approximately the same as the height of the beam at room temperature (Fig. 6). In addition, the thermocouple is placed as close to the end of the beam as possible. These steps were both taken to ensure that the thermocouple reading accurately reflected the temperature of the water near the beam. Based on the thermocouple readings, the temperature of the water decreased slowly both when being cooled and heated, so the experimental measurements were assumed to be quasi steady state. The entire apparatus has the capability to be moved in three coordinate directions. The stand height can be adjusted vertically as needed by rotating the white handle shown in the figure. The lens can be moved closer or farther from the PDMS beam using the black knobs located on the camera apparatus. Movements in the

third coordinate direction can be completed manually by shifting the metallic stand to the side by hand.
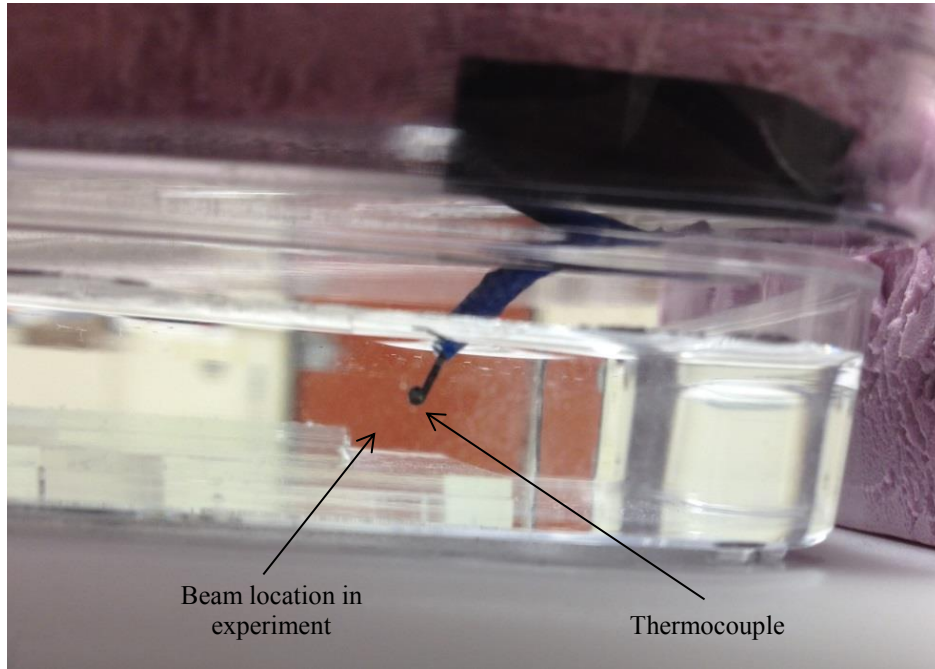
Figure 6. Image of Thermocouple Location in Pitri Dish.

Experiments were initiated by turning on the hotplate. The hotplate temperature was increased in increments of 10-15˚C. At each increment, the temperature of the thermocouple was allowed to reach a steady state value. At this point, the temperature was recorded and an image of the beam was taken using the camera. Even at a steady state temperature, the free end of the beam would shift vertically over a period of several minutes. As such, several images were taken of the beam at each steady state temperature and the average beam height was used for the deflection analysis. It is assumed that these variations were due to small liquid perturbations, potentially caused by ambient vibrations or natural convection currents. Images were taken of the beam in

fairly regular temperature increments until the hot plate temperature setting reached 85°C. This upper limit was used to ensure that no deformation of the plastic pitri dish occurred as a result of the high temperature of the hot plate, which was observed when the hotplate temperature exceeded 100°C.

B.3 Data Analysis

Each image of the beam was analyzed using ImageJ. The pixel location of the fixed and free end of the beam was recorded. The beam deflection was then taken to be the difference in height between these two locations. The resolution of the camera setup was used to convert the deflection to millimeters. The density of the water during each image was calculated using the temperature of the thermocouple near the beam [30]. The result was then plotted and compared to theoretical predictions made using simple beam theory.

B.4 PDMS Solid Properties

Reported values of the Young's Modulus of PDMS vary between 360 kPa and 3 MPA [18]. For this analysis a Young's Modulus of 1 MPA [2,4] was assumed for the theoretical calculations, which is close to the Young's Modulus of 1.32 MPa found [31] for Dow Corning Sylgard 184 cured at room temperature. It should be noted that the Young's Modulus of PDMS has been found to increase from 0.600 MPa to 1.4 MPa as the thickness of the PDMS specimen decreased from 1.8 mm to 50 μm [2]. However, these experiments [2] were completed with PDMS that was cured by heating. Since

curing the PDMS with an external heat source is known to increase the Youngs Modulus

of the PDMS [31], this result is not the best source to estimate the Youngs Modulus of

PDMS used in this experiment because the PDMS beam used here was cured at room

temperature.

B.5 Analytical Model

The theoretical deflection was estimated using simple beam theory. The beam

deflections can be predicted theoretically, since it is effectively a beam under a

distributed load due to its buoyancy force. The general equation for the deflection of a

beam under a distributed load is

$$\delta = \frac{qL^4}{8EI} \tag{7}$$

where q is the distributed load, L is the length of the beam, E is the Young's Modulus,

and I is the moment of inertia. In this case, the moment of inertia (Eq. 8) is for a

rectangular cross section and the distributed load (Eq. 9) is due to the buoyancy force

across a unit length of the beam.

$$I = \frac{1}{12}bh^3 \tag{8}$$

$$q = \rho Ag \tag{9}$$

$$A = bh \tag{10}$$

where b is the width of the beam, h is the depth of the beam, ρ is the effective density (the difference in density between the water and PDMS at a given temperature), A is the cross sectional area of the beam (Eq. 10), and g is the gravitational constant.

RESULTS AND DISCUSSION

A. Flow Experiments

Before calculating the theoretical results, the cross sections of the channels were imaged using a FEI XL 30 Scanning Electron Microscope. Some of these images are shown in Figure 7. Multiple images indicated that the sides of the channels were tapered, resulting in an increased effective width. To account for this, the width of the channel used in the theoretical model was increased. Based on the images, the angle of the taper was about 6 degrees resulting in a larger width across the top of the channel. Given this angle, the width at the top of the channel is equal to its intended width plus 20 percent (10 percent on each side) of the channel depth. The effective width was taken to be the average of the top and bottom channel width. Thus, 0.5 μm was added to the width for the channels with a depth of 5 μm, 1 μm was added to the width of all channels with a depth of 10 μm, and 1.5 μm was added to the width of all channels with a depth of 20 μm.
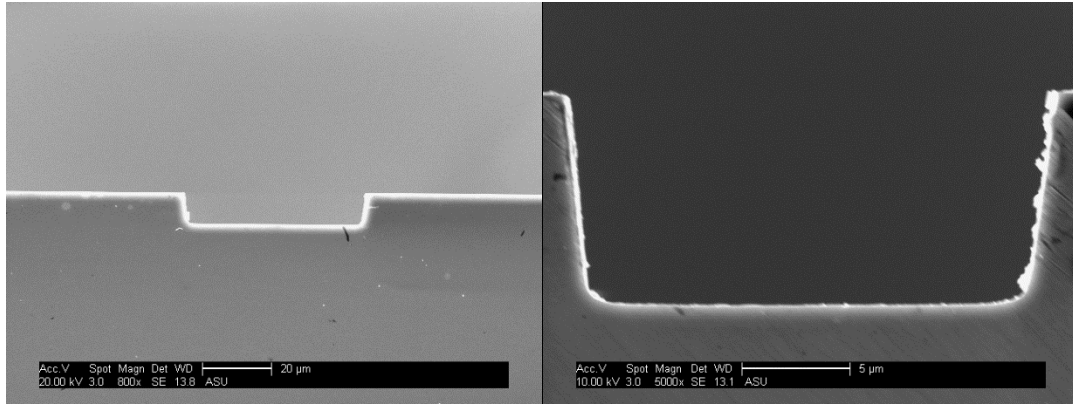
Figure 7. Cross Section of Channels taken using the SEM.

Using the method described above, the experimental flow rates and model flow rates are calculated. Values for the flow rate constant, a, is shown versus the micro channel width to depth ratio (Figs. 8-10). Note that the flow rate constant, a, (Eq. 1) shown in Figures 3 and 4 is the square root of the mobility parameter, k (Eq. 2), used in the analytical model. All values are reported for bare Silicon, HMDS coated, and PTFE coated micro channels with depths of 5, 10, and 20 μm. In Figures 8-10, image A shows data for channels with 5 μm depths, image B shows data for channels with a depth of 10 μm, and image C shows data for channels with a depth of 20 μm. In all three figures, experimental data points are green and model predictions are blue. Error bars on the experimental data are minimum and maximum values. The fit (Eq. 1, with offset) shows good agreements with the data.
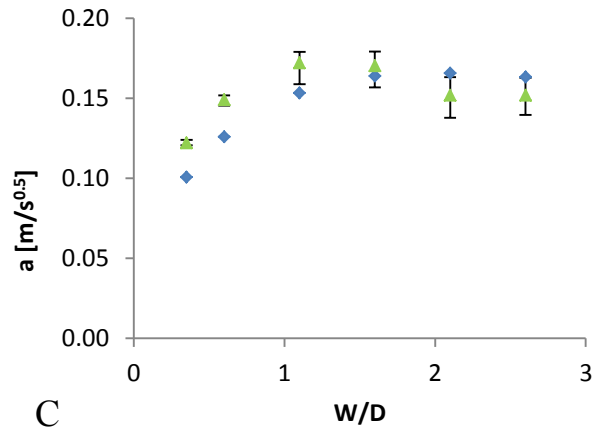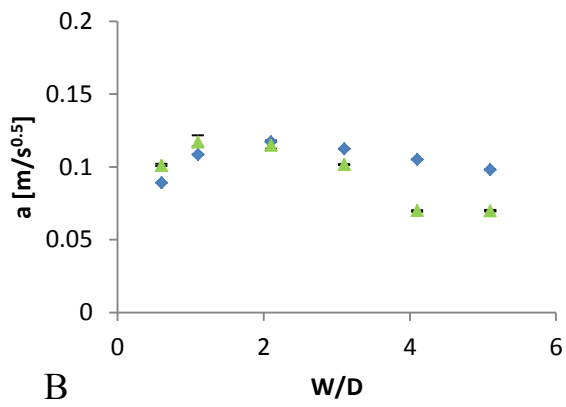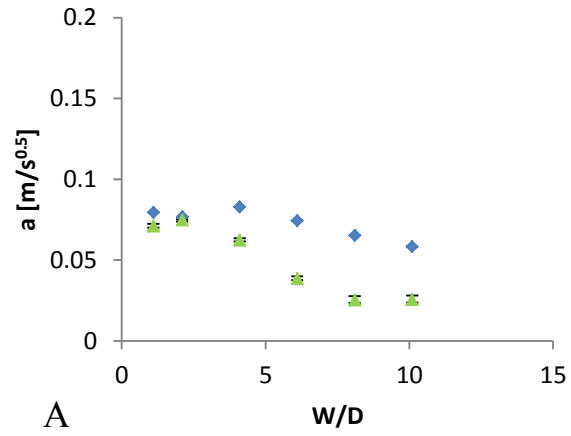
Figure 8. Flow Rate Constant, a, versus Channel Width/Depth Ratio for Silicon Wafer

A

B

C
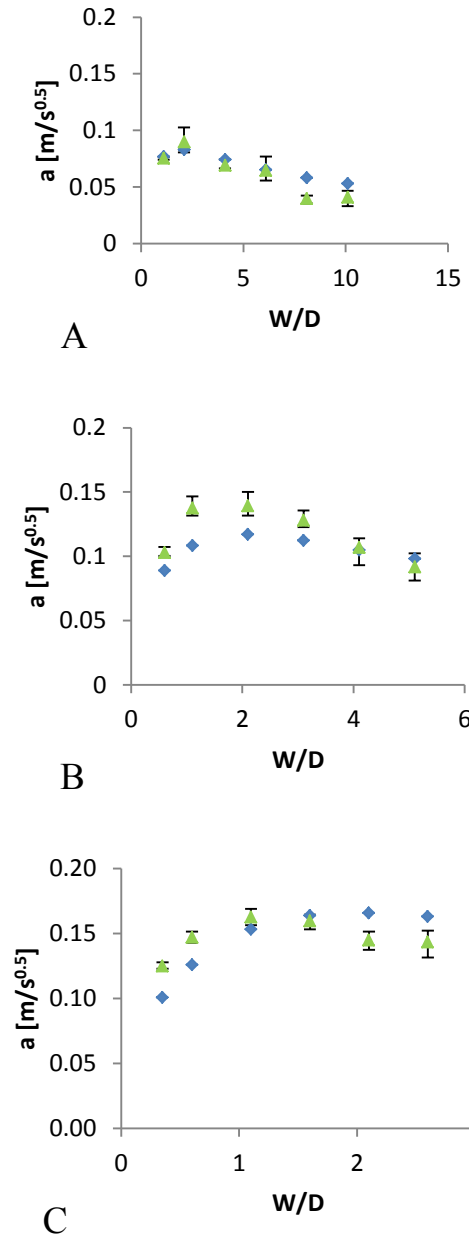
Figure 9. Flow Rate Constant, a, versus Channel Width/Depth Ratio for HMDS Wafer
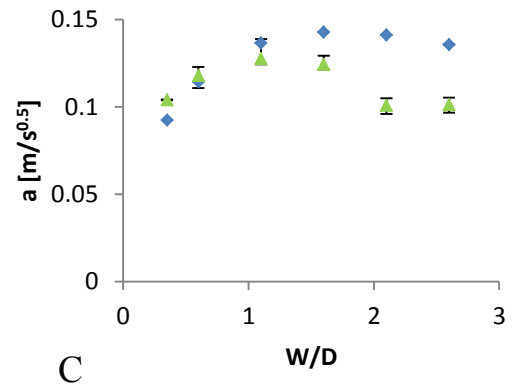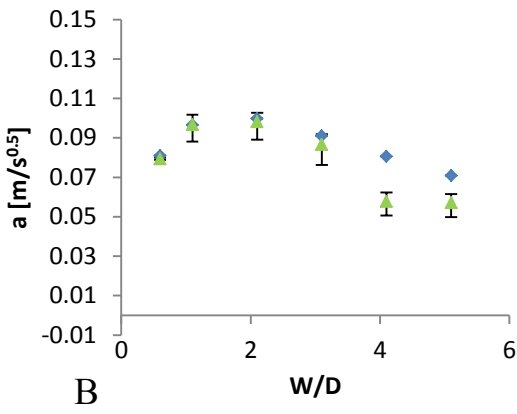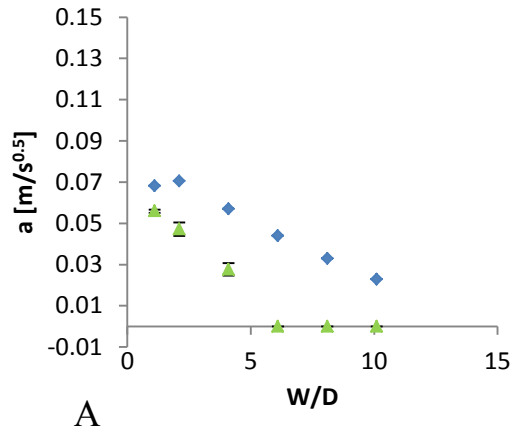
Figure 10. Flow Rate Constant, a, versus Channel Width/Depth Ratio for PTFE Wafer

Three plots of experimental data with their respective fitted equation are shown in Figure 11. Image A shows data for a PTFE coated wafer with a width and depth of 10 μm, image B shows data for a PTFE coated wafer with a depth of 20 μm and a width of 30 μm, and image C shows data for a bare Silicon wafer with a depth of 5 μm and a width of 10 μm. R^2 values are larger than 0.994 for the fits on all 153 experimental runs having non-zero flow rates.
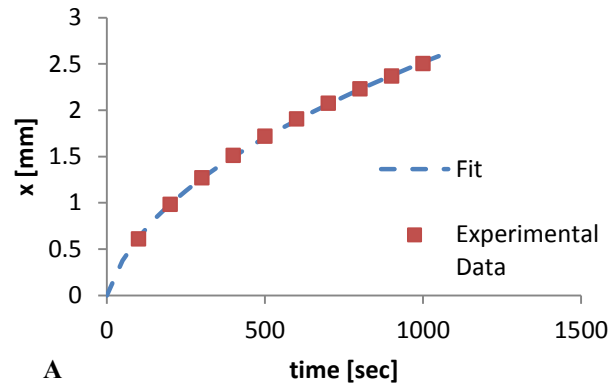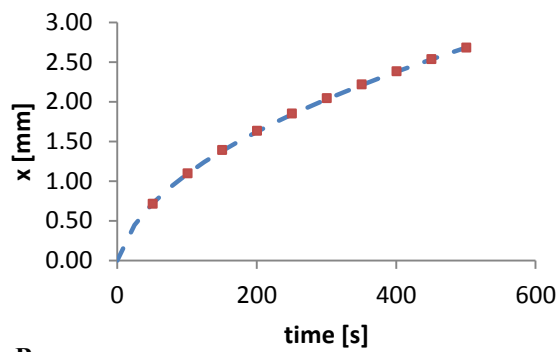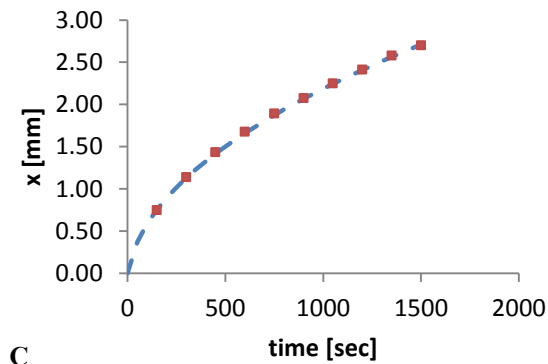
Figure 11. Experimental (red) and Theoretical (blue) Flow Distance versus Time for Three Experiments.

Flow rates on HMDS are higher than on Silicon when channel width and depth are held constant, albeit slightly. This is despite the fact that the theoretical model

predicts that the PDMS should flow through these channels at the same rate. Flow rates on the pure silicon and HMDS coated wafers are higher than flow rates on the PTFE coated wafer when width and depth are held constant. This is to be expected, due to the larger equilibrium contact angle between PDMS and a PTFE coated wafer. At a given width and depth, the flow rate on the silicon and HMDS coated wafer is generally 20-50% faster than on the PTFE coated wafer. On a given wafer, the flow rate constant, a, varies based on the aspect ratio, p. At p less than one, the fluid flow rate slows considerably. This is to be expected, since in a narrow channel viscous forces dominate resulting in slower flow rates. For very large width to depth ratios, the fluid flow rate also decreases significantly. At large width to depth ratios, an increase in the width of the channel would have a small impact on the total surface area of the channel for capillary flow, but would cause a relatively larger increase in the cross sectional area of the micro channel. As such, as the width is increased for channels with already large aspect ratios, the channels must pull significantly more fluid with a relatively small increase in capillary force, which explains the slower flow times. For both the experimental and predicted data, there exists an intermediate width to depth ratio at which the flow rate constant, a, is a maximum. This "ideal" width to depth ratio appears to be about two. The only exception is the experimental data for channels with a depth of 5 μm on the PTFE coated wafer, which will be discussed later.

Three major trends are visible when comparing the experimental and model predicted flow rate constants (Figs. 8-10). First, for p between 1 and 2, the model and experimental measurements compare favorably. Second, as the width to depth ratio increases for a given depth, the experimental results tend to lag relative to the model.

Third, for aspect ratios of less than one the flow rate is larger than that predicted by the model. This last trend is more pronounced as the width to depth ratio decreases.

Two physical phenomena could explain the decreasing flow rate as the width to depth ratio is increased. The first contribution to this trend is the forward meniscus morphology of the flow. These morphologies have been described by Seemann et al. [26] who identified distinct forward meniscus morphologies which develop in static fluids depending on the equilibrium contact angle between the solid and liquid and the depth to width ratio of the channel geometry for flow in rectangular micro channels. In the experiments described in this paper, a curved forward meniscus develops in which the fluid height gradually decreases and finger like liquid filaments protrude in front of the channel flow at the bottom corners of the channels. Due to the small distance from the channel wall to the inner finger edge, viscous forces in the fingers due to the no slip condition at the wall are large. This would result in reduced flow rates. Further, by visual observation (Fig. 12), the finger like protrusions are longer in channels with large width to depth ratios, which explains why the experimental flow rates are smaller than the model predicted flow rates by a greater magnitude as the aspect ratio becomes larger.

Figure 12. Image of PDMS Flow in Silicon Micro Channels with a Depth of 10 μm (top) and PTFE Coated Micro Channels with a Depth of 10 μm (bottom).

Three fluid morphologies identified by Seemann et al. [26] for static forward menisci occur based on the parameters chosen for these experiments. It is assumed that since these flow rates are small (0-12 μm/s), the forward meniscus profiles are similar to those identified by Seemann et al. [26], and that the transition point between different morphologies occur at similar equilibrium contact angles and width to depth ratios. In the first fluid morphology (Fig. 13e), the top meniscus is concave down (Fig. 13b) and the finger like liquid filaments fill the corners (Fig. 12c) but are not sufficiently large to become pinned (Fig. 13d) at the upper surface. This morphology occurs on the silicon and HMDS coated wafers when the width to depth ratio is smaller than 2 and on the PTFE coated wafer when the width to depth ratio is smaller than about 3.3. In the second fluid morphology (Fig. 13f) the top fluid surface is also concave down, although the filaments have become sufficiently large to become pinned at the upper corner of the

micro channel. It is conceivable that the pinning of the filament results in decreased flow rates due to an increase in flow resistance. This morphology occurs on the silicon and HMDS coated wafer for width to depth ratios larger than 2, assuming the equilibrium contact angle is equal to zero, and on PTFE coated wafers when the width to depth ratio is larger than 3.3 but smaller than about 7. For the third fluid morphology (Fig 13g), the top surface is concave up (Fig. 13a) and the liquid filaments are sufficiently large to become pinned to the upper corner of the micro channel. This fluid morphology only occurs on PTFE coated wafers with width to depth ratios larger than about 7, given an equilibrium contact angle of 30.4° for liquid PDMS on a PTFE coated surface. The flow rate is effectively zero for this fluid morphology.

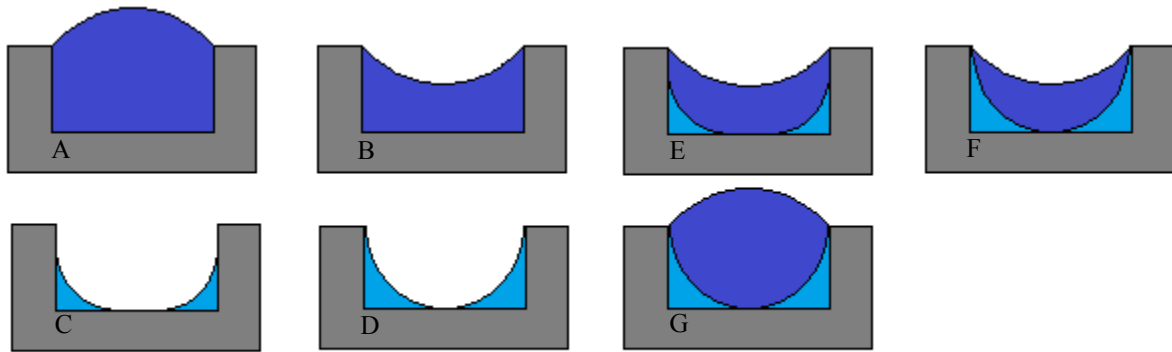Figure 13. Forward Meniscus Profiles taken directly from Seemann et al. [26]

The second physical phenomena which explains the decreasing flow rate relative to the model is the existence of a curved top fluid surface, which is predicted by the work of Seemann et al. [26] for all the channel geometries used in these experiments when the fluid velocity is non-zero. A top surface with a curvature oriented concave to the inside

of the channel would have larger fluid viscous forces, due to the smaller distance between the channel walls and the top edge of the fluid. This effect is most noticeable when looking at channels with small width to depth ratios. As mentioned above, experimental flow rates are generally higher than model predicted flow rates at low width to depth ratios. However, for shallow channels with a depth of 5 μm, this breaks down. The actual flow speed is slower than the model predicted value. For channels with a depth of 10 μm, the experimental and predicted values are similar, while for the deepest channels the experimental flow rate is much faster than that predicted by the model. This behavior is consistent with the effect of a curved top meniscus. The drop in fluid height at the top surface would be independent of the depth of the channel. As a result, the fluid would be slowed significantly in shallow channels, whereas in deeper channels the reduction in height would cause a negligible change in the channel cross section.

One notable aspect of PDMS flow behavior in these experiments is the non-existent flow rate constant recorded for channels with 30, 40, and 50 μm widths on PTFE coated wafers with a depth of 5 μm. For these experiments, only the finger like protrusions advanced into the channels. The 40 and 50 μm width channels have width to depth ratios larger than 7, and so are in the third forward meniscus morphology described above. It is assumed here that the channel with a 30 μm width is also in this fluid regime, even though the width to depth ratio for this channel (6.1) is just under the transition width to depth ratio of 7. The discrepancy could be a result of error in the contact angle measurements. Zero fluid forward movement in this regime is consistent with the work [26] that defined these morphologies and multiple experimental studies [32-35] in which fluid is made to extend or retract in microfluidic channels by changing its forward

meniscus morphology by using electrowetting to control the fluid contact angle. The negligible fluid velocity at the boundary (p of 6 on PTFE) between the two forward meniscus morphologies could also result from the combination of the physical parameters being close to the third morphology and the effect of the slanted channel side walls.

There are two possible explanations for the faster fluid flow at aspect ratios of less than one. First, it is well documented in the review paper by Hatzikiriakos [35] that polymer melts will slip at wall surfaces under various conditions. Slip has been observed in higher viscosity PDMS at shear rates as low as 40 s^{-1} at 30°C [36]. Further, Kaylon et al.[36] state that slip may in fact occur at lower shear rates than measured in their experiments because slip was observed using a visual method having a low resolution and because the flow was observed over only 13 strains. Due to the slow flow rate in these micro channels, shear rates are generally small. However, for the narrowest channels the combination of faster flow rates (~4-12 μm/s) and small channel widths produce non-negligible shear rates. Shear rates on bare silicon, HMDS coated, and coated PTFE coated wafers with a depth of 20 μm and a width of either 5 or 10 μm vary between roughly 1 and 10 s^{-1} over the course of an experiment, assuming a velocity profile in which there is no slip at the walls. It should be noted that experiments measuring wall slip of Dow Corning Sylgard 184 could not be found in the literature. In addition, the degree of slip in PDMS specifically has been shown to vary depending on the strength of liquid surface interactions [37], so slip in these experiments would occur at different shear rates than those measured by Kaylon et al.[36]. Despite this, the work done by Kaylon et al. suggests the possibility that a small amount of slip is occurring near the wall in these micro channels, which could partially or completely explain the faster

than predicted flow rates. Second, it is possible that surface roughness could artificially increase the surface area in the micro channel, which would result in a larger change in interfacial energy per unit distance traveled by the flow. A resultant increase in the capillary driving force would cause faster flow rates. This effect would be larger in narrow channels since the ratio of the channel surface area to channel cross sectional area is larger. Further experiments would be necessary to verify the validity of these explanations, but are outside the scope of this paper.

It was observed earlier that for values of p between 1 and 2 the experimental and model predicted flow rates compare favorably. It can be concluded that in this intermediate range of p, the phenomena causing faster or slower flow are either both significant but together have no net effect on the flow rate or that they are both individually insignificant. Lastly, the difference in flow rates between bare Silicon and HMDS wafers should be addressed. This is likely due to differences in the dynamic contact angle of PDMS on these two surfaces. Further experiments would be necessary to quantify this difference and evaluate its effect on the flow rate of PDMS on these two surfaces.

B. Deflection Experiments

A full loading and unloading experiment was completed for a beam cured in a channel with a depth of 10 μm and a width of 20 μm. For this experiment, the deflection of the beam was tracked while the temperature of the water was increased to about 60˚C

and also as it decreased back to room temperature by unforced heat rejection to the ambient.

The initial results are shown in Figure 14. Beam deflection is shown as a function of the water density, which was calculated based on the temperature of the water at the time the image was taken. The beam deflection as the temperature was increased is shown in blue while the beam deflection as the temperature was decreased is shown in red. The water initially began at a density of approximately 0.996 g/cm^3, and as it was heated the density decreased. After the density reached a minimum of 0.984 g/cm^3 (~60°C), the water was allowed to cool back to room temperature.
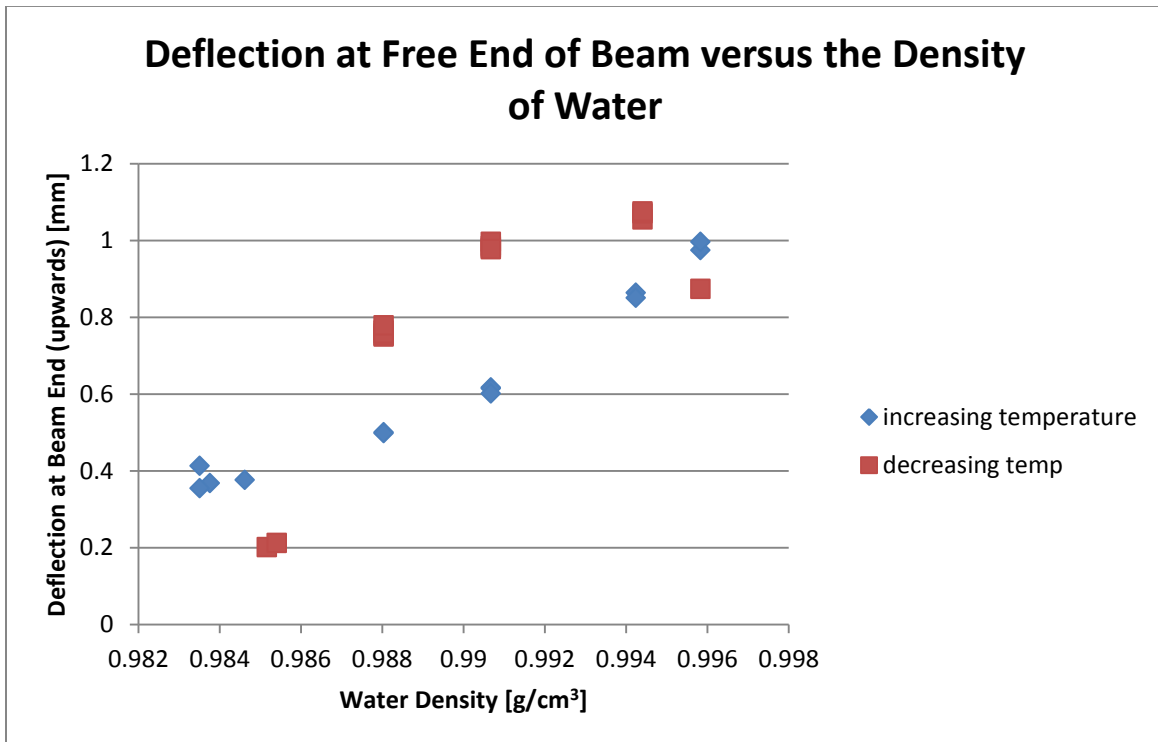
Figure 14. Plot of Beam Deflection during the Load/Unload Test.

The general load and unload trend in Figure 14 is apparent. The beam deflection decreases as the water density decreases. This is because as the density decreases, the effective density differential between the water and PDMS decreases, reducing the upward buoyancy force on the beam. A total decrease in the deflection of the beam of about 0.8 mm is recorded in this experiment. As the temperature of the water is allowed to cool, the beam deflection increases and nearly returns to its original location. Although there is significant noise, the expected loading and unloading behavior is clear. Note that the change in water density between each data point is about 0.004 g/cm^3. Thus, the change in buoyancy force on the beam will be

$$F_B = \rho g V \tag{11}$$

where g is the gravitational constant and V is the volume of the beam, with

$$V = Lbh \tag{12}$$

where L being the length of the beam, b being the beam width, and h being the beam height. Using this equation and the dimensions of the beam used in this experiment, the change in buoyancy force across the range of water densities at which the beam deflection was measured (0.996-0.984 g/cm^3) is only 65.8 pN, or approximately 16.4 pN per data step.

Experimental and Theoretical Results for the Deflection of the Free End of the Beam versus the Density of Water

y = 9.0354x - 8.0229
R² = 1

y = 56.722x - 55.423
R² = 0.6856

- ◆ experimental deflection curve
- ▲ theoretical deflection curve
- —— Linear (experimental deflection curve)
- —— Linear (theoretical deflection curve)

Deflection (upwards) [mm]

Water Density [g/cm³]
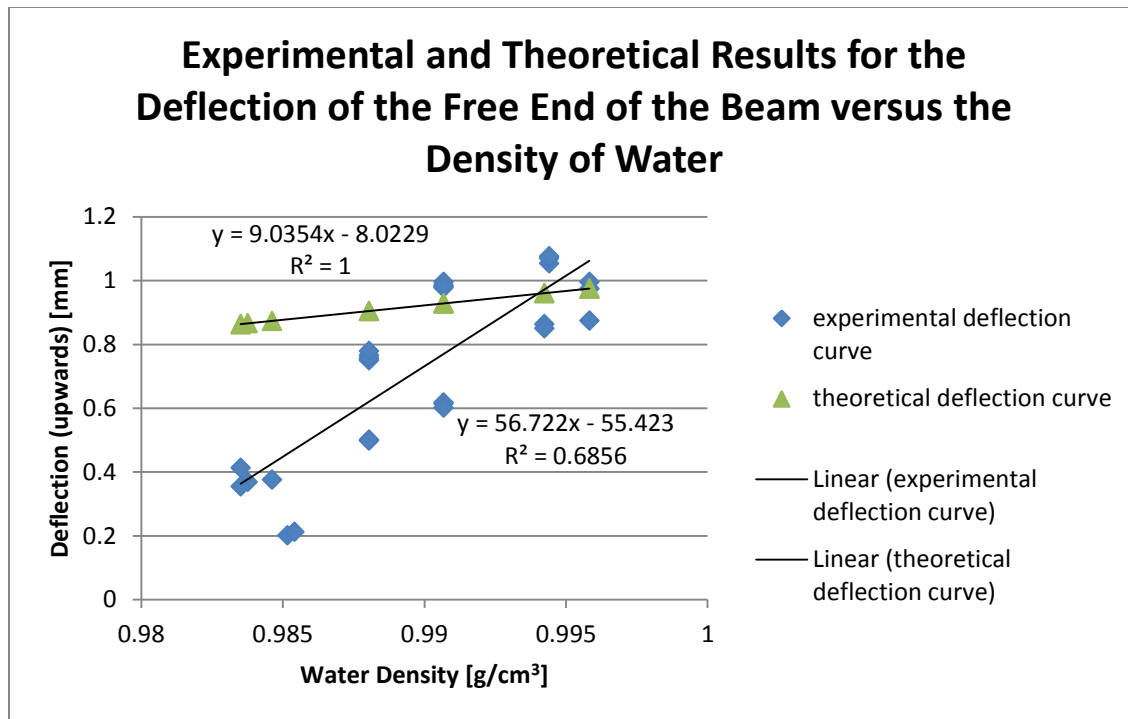
Figure 15. Comparison of Load/Unload Experiment to Theoretical Predictions.

Figure 15 shows the experimental data plotted with the predicted deflection data that was calculated using equations 7-10. The beam was assumed to have the same dimensions was the channel in which the PDMS cured. Again, for this beam the channel had a depth of 10 μm and a width of 20 μm. In addition, the Young's modulus of PDMS was assumed to be 1 MPa, as is explained in the experimental methods section. Based on the beam image, the beam length was approximately 2.8 mm. A linear fit was applied to the experimental loading and unloading data. This was compared to the predicted data, to which a linear fit was also applied. Based on the linear fits, the experimental deflection from a given density change was larger than the deflection predicted by theory by a factor of six.

Although the magnitude of the experimental deflection of the beams is at the predicted order of magnitude, a six fold difference between experimental and theoretical predictions requires explanation. There are a variety of potential sources of error in this experiment.

First, ambient vibrations could be a significant source of error. Beam movements on the order of tenths of a millimeter were clearly observed while setting up the experiment merely from the miniscule vibration introduced from "clicking" a computer mouse located on the vibration insulated table on which the experiments were conducted. During the course of the experiment, the mouse was moved off the table. However, vibrations from the computer located on the table or ambient air movements from the air conditioning system could have been a source of error, given the sensitivity of the setup. Although this source of error could have introduced significant random noise into the data set, it isn't conceivable for it to have been the cause of the larger than expected experimental beam deflections. This error could be mediated in the future by moving the computer off the table, or introducing a vibration resistant media into the experimental setup.

Second, there could be error in the temperature measurements of the water near the beam. The temperature reading of the thermocouple generally reads below the temperature of the hot plate by approximately 15°C, indicating the presence of a significant temperature gradient in the water. Although the thermocouple was located close to the beam end, it isn't possible to directly measure the temperature of the water exactly at the beam. Further, the temperature of the water near at the beam, and thus its density, may not be constant across the beam length. This source of error could cause a

uniform shift in the thermocouple temperature reading relative to the actual water temperature near the beam. However, it is not possible that this error is the cause of the deviation between experimental and theoretical deflections, since there is no temperature at which liquid water at atmospheric pressure has a low enough density (~0.930 g/cm^3) [30] to cause the large deflections recorded in the experiment. Nonetheless, the degree of this source of error could be determined by introducing more thermocouples into the experimental setup in future experiments. Further, the presence of temperature gradients could be reduced by introducing additional insulation.

Third, unintended beam deflections could be caused by natural convection within the water. These natural convection currents would be caused by the temperature gradients in the water and would create a drag force on the beam, causing it to deflect. Anticipating the magnitude and direction of these currents in these experiments would be inordinately complex. However, it is possible to roughly estimate the fluid velocity necessary to create a drag force on the beam that would have an order of magnitude similar to the buoyancy force acting on the beam. The drag force of a moving fluid on a solid body can be described by

$$F_D = \frac{1}{2}\rho C_D A_D v^2 \qquad\qquad (13)$$

where ρ is the density of the fluid, C_D is the drag coefficient, A_D is the cross sectional area of the object subject to the vertical water flow due to natural convection, and v is the fluid velocity. The density of water can be approximated as 1000 kg/m^3 and the area is the beam length (3 mm) multiplied by the beam width (20 μm). The drag coefficient is

unknown, but since this analysis is an estimate only of the order of magnitude of fluid velocity at which drag forces would be significant, a drag coefficient on the order of one will be assumed as an approximation. The net force on the beam can be calculated using equation 13. Setting the two forces equal and plugging in the relevant values for the variables gives

$$5.88 * 10^{-11} = 0.00003v^2 \tag{14}$$

which reduces to

$$v = 1.4\ mm/s \tag{15}$$

Again, it would be difficult to estimate the fluid velocity due to natural convection analytically. However, given the fact that this velocity is relatively low, it is not inconceivable that buoyancy induced natural convection currents exert non-negligible forces on the beam. This effect could potentially be reduced with better insulation. Insulating materials would reduce the magnitude of any temperature gradients, which in turn would reduce the magnitude of buoyancy induced natural convection.

Fourth, deviations in the beam geometry could be a source of error. For the theoretical prediction of beam deflection, it was assumed that the beam geometry would be the same as the channel in which it cured. In the case of the experiment mentioned above, the depth of the channel was 10 μm while the width of the channel was 20 μm. This assumption may not be accurate. When the PDMS flows into the channel, is does

not fill the channel completely due to the top meniscus described in Figure 12b. In addition, it is possible that the PDMS contracts slightly when it is removed from the channel. Since the deflection of the beam varies with the square of the beam depth, this could have a large impact on the total beam deflection.

To investigate this, several images of beam cross sections were taken using a Focused Ion Beam Electron Microscope (FEI NOVA). These beams were created using the same method as the beam used in the deflection experiment. However, the device was placed on a small piece of Silicon instead of the substrate used in the experiments. The beams were cut using a razor blade. Images of the beam cross sections were taken in the electron microscope. Each beam that was imaged was cured in a channel with a width and depth of 20 μm. Four cross sections were imaged. The images are shown in Figure 16.
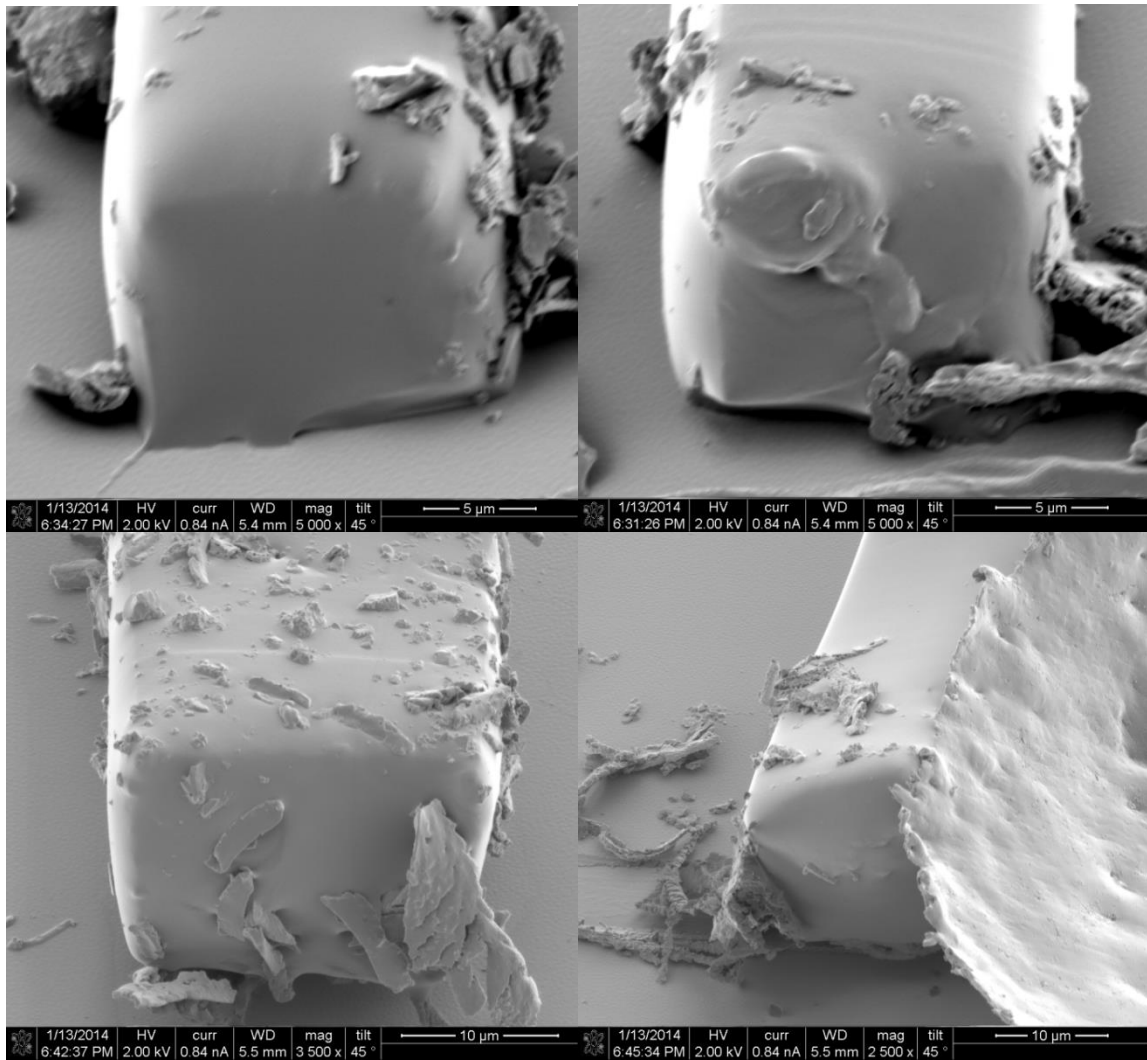
Figure 16. Image of Four Beam Cross Sections removed from Wafer.

The scale bars at the bottom can be used to estimate the actual height of each beam. Each image was taken at an angle of 45°, so to estimate the height of a given cross section the height shown on the picture must be multiplied by the square root of two. It is difficult to estimate the cross section of the beams accurately because of the viewing angle, but from a visual inspection the top two images in Figure 15 appear to have heights that are closer to 15 µm while the bottom two cross sections appear to have

heights closer to 20 µm. All the beams appear to have widths closer to 15 µm (note that the width measurement does not have to be adjusted by a factor of radical two). Although these images are not conclusive, they indicate that the beam shape undergoes some deformation when it is removed from the wafer. Further images would be necessary to determine the extent of these deformations. For these images, the beams should be oriented so that the microscope is oriented normal to the face of the beam, instead of at a 45° angle. Images could also be taken of cured PDMS that has not been removed from the channel, in order to quantify the height of the curved top meniscus. These images could be useful for future work involving both the flow and deflection experiments.

Fifth, uncertainty in the physical properties of the PDMS beams could be a source of error. The range of values for the Young's Modulus of PDMS was discussed in the experimental methods section of this result. The deflection is linearly related to the Young's Modulus, so it is not reasonable for this to be the source of the six fold difference between the experimental and theoretical results. However, errors on the order of 25-40% are conceivable. Further, measurements of the actual length of the PDMS beam in a given experiment could also be a source of error. The beams are designed to have a length of 3mm, but they are cut by hand using a razor so deviations from this value are expected. After being cut, the length of the beam is estimated using the image of the beam under the microscope and the resolution of the microscope setup. However, if the beam has significant bending in the direction of the camera, the length could be underestimated. The deflection of the beam is proportional to the length of the beam to the power of four. If the beam is assumed to have a length only 15% smaller than its

actual length, the theoretical deflection calculated will underestimate the beam's true theoretical deflection by a factor of two. If the beam length is underestimated by an admittedly large 35%, the six fold variation between the experimental and theoretical results would be completely explained. Further, this type of movement is observed often while setting up an experiment, so it is a particular concern as a source of error. Sideways beam movement could be caused by natural convection currents, ambient vibrations, or residual stresses in the beam from the curing process. One method to make measurements of the beam length more accurate would be to place features along the beam length at known intervals that could function as markers for the beam length.

CONCLUSION

In the first part of this work, a comprehensive study of the flow of PDMS in open rectangular micro channels with a range of depths and widths, in either pure silicon, HMDS coated, or PTFE coated channels, has been completed. The experimental flow rates were compared to an analytical model [24] based on the work of Lucas and Washburn [19,20]. Experimental and predicted flow rates agree strongly for channels with width to depth ratios between one and two. Flow rates in channels with width to depth ratios less than one were higher than predicted by the model, while flow rates in channels with width to depth ratios greater than two were significantly slower than predicted, particularly as the aspect ratio was increased. Several rules of thumb for the design of PDMS based microcantilever devices can be inferred from these results. First, channels with aspect ratios near two should be incorporated into the device as often as

possible to ensure full impingement of PMDS into the device mold. Second, the channel geometries determined by Seemann et al. [26] which would result in zero PDMS impingement should clearly be avoided. Third, channel width to depth ratios larger than three should be used sparingly. This is of particular importance, since a large width to depth ratio could be incorporated into the design with the purpose of reducing the device stiffness in directions perpendicular to the desired measurement direction.

In the second part of this work, a preliminary experimental setup for calibration tests on ultrasensitive PDMS cantilever beams is reported. One loading and unloading cycle is completed on a microcantilever PDMS beam with a length of about 2.8 mm, a depth of 10 μm, and a width of 20 μm. Beam deflections are actuated by adjusting the buoyancy force on the beam, which is submerged in water. The buoyancy force is adjusted by increasing the temperature of the water. The results show the general trend expected for a loading and unloading cycle, albeit with significant experimental error. The error is a result of the extreme sensitivity of the beam, which based on its design should have a theoretical stiffness of about 0.5 pN/μm when subjected to the distributed load caused by buoyancy forces, according to Euler beam theory. The experimental results indicate that the beam stiffness is a factor of six larger than predicted theoretically. One probable explanation is that the beam geometry shrinks when it is removed from the channel after curing, making assumptions about the beam geometry used in the theoretical analysis inaccurate. This theory is partially bolstered by images taken of beams that have been removed from the channel in which they were cured. Images of these beams' cross sections captured using an electron microscope showed mixed results, so future work is necessary to determine the viability of this explanation. A second

probable explanation is that errors in estimating the beam length are causing artificially small theoretical beam deflections. Several other sources of error which could also partially contribute to the divergent results are described. Improvements to the experimental setup that could mitigate the effect of these sources of error in future experiments are suggested.

REFERENCES

[1] Quake, S.; Sherer, A. From Micro- to Nanofabrication with Soft Materials. *Science* **2000**, 290, 1536-1540.

[2] Liu, M.; Sun, J.; Sun, Y.; Bock, C.; Chen, Q. Thickness-dependent mechanical properties of polydimethylsiloxane membranes. *J. Micromech. Microeng.* **2009**, 19, 035028. DOI:10.1088/0960-1317/19/3/035028

[3] Dow Corning. "Product Information: Sylgard® 184 Silicone Elastomer." 2014, from http:// www4.dowcorning.com/DataFiles/090007c8804076af.pdf

[4] Rajagopalan, R.; Saif, T. A. Fabrication of Freestanding 1-D PDMS Microstructures Using Capillary Micromolding. *J. Microelectromech. Syst*. **2013**, 22, 992-994.

[5] Zhao, Y.; Zhang, X. Adaptation of flexible polymer fabrication to cellular mechanics study. *Appl. Phys. Lett*. **2005**, 87, 144101. DOI:10.1063/1.2061861

[6] Tan, J.; Tien, J.; Pirone, D.; Gray, D.; Bhadriraju, K.; Chen, C. Cells lying on a bed of microneedles: An approach to isolate mechanical force. *Proc. Natl. Acad. Sci. U. S. A*. **2003**, 100, 1484-1489. DOI: 10.1073/pnas.0235407100

[7] Harris, A. K.; Stopak, D.; Wild, P. Fibroblast traction as a mechanism for collagen morphogenesis. *Nature* **1981**, 290, 249-251.

[8] D. Kim, K. W. Pak, J. Park, A. Levchenko, and Y. Sun. Microengineered platforms for cell mechanobiology. Annu. *Rev. Biomed. Eng*. **2009**, 11, 203–233. DOI: 10.1146/annurev-bioeng-061008-124915

[9] J. Rajagopalan and M. T. A. Saif. Mems sensors and microsystems for cell mechanobiology. *J. Micromech. Microeng*. **2001**, 21, 054002-054012. DOI: 10.1088/0960-1317/21/5/054002

[10] Nezhad, A. S.; Chanbari, M.; Agudelo, C. G.; Packirisamy, M.; Bhat, R. B.; Geitmann, A. PDMS Microcantilever-Based Flow Sensor Integration for Lab-on-a-Chip. *IEEE Sens. J*. **2013**, 13, 601-609.

[11] Ungar, M. A.; Chou, H.; Thorsen, T.; Sherer, A.; Quake, S. Monolithic Microfabricated Valves and Pumps by Multilayer Soft Lithography. *Science* **2000**, 288, 113-116.

[12] G. M. Whitesides, E. Ostuni, S. Takayama, X. Jiang, and D. E. Ingber. Soft lithography in biology and biochemistry. *Annu. Rev. Biomed. Eng*. **2001**, 3, 335–373. DOI: 10.1146/annurev.bioeng.3.1.335

[13] R. Bashir. Biomems: State-of-the-art in detection, opportunities and prospects. *Adv. Drug Deliver Rev.*, **2004**, 56, 1565–1586. DOI: http://dx.doi.org/10.1016/ j.addr.2004.03.002

[14] Williams, B. J.; Sandeep, A. V.; Rajagopalan, J.; Saif, T. A. A self-propelled biohybrid swimmer at low Reynolds number. *Nat. Commun.* **2013**, 5, 3081 DOI: 10.1038/ncomms4081

[15] Enoch, K.; Xia, Y.; X., Whitesides, G. M. Polymer microstructures formed by moulding in capillaries. *Nature* **1995**, 376, 581-584. DOI: 10.1038/376581a0

[16] Enoch, K.; Xia, Y.; Whitesides, G. M. Micromoulding in Capillaries: Applications in Materials Science. *J. Am. Chem. Soc.* **1996**, 118, 5722-5731 DOI: 10.1021/ja960151v

[17] Rajagopalan, J.; Tofangchi, A.; Saif, M. T. A. Linear High-Resolution BioMEMS Force Sensors With Large Measurement Range. *J. Micromech. Syst.* **2010**, 19, 1380-1389 DOI: 10.1109/JMEMS.2010.2076780

[18] Cappelleri, D. J.; Piazza, G.; Kumar, V. A two dimensional vision-based force sensor for microrobotic applications. *Sens. Actuators, A*, **2011**, 171, 340-351 DOI: 10.1016/j.sna.2011.06.014

[19] Washburn, E. W. The Dynamics of Capillary Flow. *Phys. Rev.* **1921**, 17, 273-283 DOI: 10.1103/PhysRev.17.273

[20] Lucas, R. Ueber das Zeitgesetz des kapillaren Aufstiegs von Flussigkeiten. *Kolloid Zeitschrift.* **1918**, 23, 15-22. DOI: 10.1007/BF01461107

[21] Ryu, W.; Huang, Z.; Park, J. S.; Moseley, J.; Grossman, A. R.; Fasching, R. J.; Prinz, F. B. Open micro-fluidic system for atomic force microscopy-guided in situ electrochemical probing of a single cell. *Lab Chip.* **2008**, 8, 1460-1467. DOI: 10.1039/B803450H

[22] Ouali, F. F.; McHale, G.; Javed, H.; Trabi, C.; Shirtcliffe, N. J.; Newton, M. I. Wetting considerations in capillary rise and imbibition in closed square tubes and open rectangular cross-section channels. *Microfluid. Nanofluid.* **2013**, 15 309-326. DOI: 10.1007/s10404-013-1145-5

[23] Girardo, S.; Palpacelli, S.; De Maio, A.; Cingolani, R.; Succi, S.; Pisignano, D. Interplay between Shape and Roughness in Early-State Microcapillary Imbibition. *Langmuir.* **2012**, 28, 2596-2603. DOI: 10.1021/la2045724

[24] Yang, D.; Krasowska, M.; Craig, P.; Popescu, M. N.; Ralston, J. Dynamics of Capillary-Driven Flow in Open Microchannels. *J. Phys. Chem*. C. **2011**, 115, 18761-18769 (2011). DOI: 10.1021/jp2065826

[25] Nilson, R.H.; Tchikanda, S.W.; Griffiths, S.K.; Martinez, M. J. Steady evaporating flow in rectangular microchannels. *Int. J. Heat Mass Transfer*. **2006**, 49, 1603-1618 (2006) DOI: 10.1016/j.ijheatmasstransfer.2005.11.002

[26] Seemann, R.; Brinkmann, M.; Kramer, E. J.; Lange, F. F.; Lipowsky, R. Wetting morphologies at microstructured surfaces. *Proc. Natl. Acad. Sci. U. S. A*. **2005**, 102, 1848-1852. DOI:10.1073/pnas.0407721102

[27] Schneider, F.; Draheim, J.; Kamberger, R.; Wallrabe, U. Process and material properties of polydimethylsiloxane (PDMS) for Optical MEMS. *Sens. Actuators, A* **2009**, 151, 95-99. DOI: 10.1016/j.sna.2009.01.026

[28] Robinson, A. P.; Minev, I.; Graz, I. M.; Lacour, S. P. Microstructured Silicone Substrate for Printable and Stretchable Metallic Films. *Langmuir*. **2011**, 27, 4279-4284. DOI: 10.1021/la103213n

[29] Parkinson, L.; Sedev, R.; Fornasiero, D.; Ralston, J. The terminal rise velocity of 10-100 μm diameter bubles in water. *J. Colloid Interface Sci.* **2008**, 322, 168-172. DOI: 10.1016/j.jcis.2008.02.072

[30] Senese, F. A. "Water Density Calculator." 2005, from http://antoine.frostburg.edu/ chem/senese/javascript/water-density.html

[31] Johnston, I. D.; McCluskey, D. K.; Tan, C. K. L.; Tracey, M. C. Mechanical characterization of bulk Sylgard 184 for microfluidics and microengineering. *J. Micromech. Microeng*. **2014**, 24, 035017. DOI:10.1088/0960-1317/24/3/035017

[32] Baret, J.; Decre, M.; Herminghaus, S.; Seemann, R. Electroactuation of Fluid Using Topographical Wetting Transitions. *Langmuir* **2005**, 21, 12218-12221. DOI: 10.1021/la052228b

[33] Baret, J.; Decre, M. J.; Herminghaus, S.; Seemann, R. Transport Dynamics in Open Microfluidic Grooves. *Langmuir* **2007**, 23, 5200-5204. DOI: 10.1021/la063584c

[34] Khare, K.; Harminghaus, S.; Baret, J.; Law, B.; Brinkmann, M.; Seemann, R. Switching Liquid Morphologies on Linear Grooves. *Langmuir* **2007**, 23, 12997-13006 DOI: 10.1021/la701899u

[35] Hatzikiriakos, S. G. Wall slip of molten polymers. *Prog. Polym. Sci*. **2012**, 37, 624-643. DOI: 10.1016/j.progpolymsci.2011.09.004

[36] Kalyon, D. M.; Gevgilili, H. Wall slip and extrudate distortion of three polymer melts. *J. Rheol*. **2003**, 47, 683-699. DOI: 10.1122/1.1562156

[37] Migler, K. B.; Hervet, H.; Leger, L. Slip Transition of a Polymer Melt under Shear Stress. *Phys. Rev. Lett*. **1993**, 70, 287-90. DOI: http://dx.doi.org/10.1103/PhysRevLett.70.287

APPENDIX A

A   MATLAB Code used for Flow Analysis

```matlab
%w50 start_point=[ ; ; ]; fimg=; limg=; NO FLOW
%w40 start_point=[ ; ; ]; fimg=; limg=; NO FLOW
%w30 start_point=[ ; ; ]; fimg=; limg=; NO FLOW
%w20 start_point=[84.5625  645.5625; 1 1; 1 1]; fimg=185; limg=1895;
%w10 start_point=[84.5625  743.3125; 1 1; 1 1]; fimg=140; limg=1895;
clear
start_point = [84.5625  645.5625; 1 1; 1 1];
base_points = [84.5625  645.5625; 1 1; 1 1];
input_points = [84.5625  645.5625; 1 1; 1 1];
%note that only the first points are set from this, the image on the
right
%after starting the program will not be set correctly, since it is the
%second image in the set
fimg = 140;
limg = 1895;
x0 = imread('PTFE d5 big 5, 0140.jpg');
y0 = .2989*x0(:,:,1) +.5870*x0(:,:,2)+.1140*x0(:,:,3);
y(:,:,1) = base_points;
for i=(fimg+1):limg
s = int2str(i);
if i<10
    filename = ['PTFE d5 big 5, 000' s '.jpg'];
elseif i>=10 && i<100
    filename = ['PTFE d5 big 5, 00' s '.jpg'];
elseif i>=100 && i<1000
    filename = ['PTFE d5 big 5, 0' s '.jpg'];
else
    filename = ['PTFE d5 big 5, ' s '.jpg'];
end
x1 = imread(filename);
y1 = .2989*x1(:,:,1) +.5870*x1(:,:,2)+.1140*x1(:,:,3);

if i==(fimg+1)
    [input_points, base_points] = cpselect(y1,y0, input_points,
base_points, 'Wait', true);
    y(:,:,fimg+1) = base_points;
end

    corrected_inputs = cpcorr(input_points, base_points,y1,y0);
    yo = y1;
    y(:,:,i+1) = corrected_inputs;
    input_points = corrected_inputs;


if rem(i,100)==0
    i
    y(:,:,i)
end

end
%y(:,:,1) = base_points;
```

```matlab
%rewrite y to vector z to remove zero elements from the array
z=zeros(3,2,limg-fimg+1);
z(:,:,1)=y(:,:,1);
j=1;
for i=(fimg+1):limg
    z(:,:,j)=y(:,:,i);
    j=j+1;
end


%calculate distance traveled by PDMS using location data in z
lengthdist=limg-fimg+1;
dist=zeros(lengthdist-1,4);
j=1;
for i=1:(limg-fimg)
    dist(i,1)=sqrt((z(1,1,i)-z(1,1,1)).^2+(z(1,2,i)-z(1,2,1)).^2);
    dist(i,2)=sqrt((z(2,1,i)-z(2,1,1)).^2+(z(2,2,i)-z(2,2,1)).^2);
    dist(i,3)=sqrt((z(3,1,i)-z(3,1,1)).^2+(z(3,2,i)-z(3,2,1)).^2);
end

%calculate true capillary flow point by finding "centroid" of flow
meniscus
%triangles
for i=1:(limg-fimg)
    avgpoint2and3=(dist(i,2)+dist(i,3))/2;
    dist(i,4)=(2*dist(i,1)+avgpoint2and3)/3;
end

%change distance vector from pixels to mm
%if 20x, convertpix2mm=0.002649
%if 50x, convertpix2mm=0.001057
convertpix2mm=0.002649;
dist=dist*convertpix2mm;

%plot distance vs time
time=0:(limg-fimg-1);
plot(time,dist(:,1),time,dist(:,2),time,dist(:,3),time,dist(:,4))
```